

# Eco-friendly and cost-effective adsorbent derived from blast furnace slag with black liquor waste for hazardous remediation

Ahmed H. Naggar (✉ [ahayoub@ju.edu.sa](mailto:ahayoub@ju.edu.sa))

Al-Jouf University College of Science <https://orcid.org/0000-0001-5492-6114>

Abdelghaffar Dhmees

EPRI: Egyptian Petroleum Research Institute

Tarek A. Seaf-Elnasr

Al-Jouf University College of Science

Kwok F. Chong

University Malaysia Pahang: Universiti Malaysia Pahang Al-Sultan Abdullah

Gomaa A.M. Ali

Al-Azhar University - Assiut Branch

Hazim M. Ali

Al-Jouf University College of Science

Rasmih M. Kh. Alshamery

Al-Jouf University College of Science

Lubna H. M. AlNahwa

Al-Jouf University College of Science

Al-Sayed A. Bakr

EPRI: Egyptian Petroleum Research Institute


---

## Research Article

**Keywords:** Sugarcane bagasse, blast furnace slag, black liquor, thorium, wastewater treatment

**Posted Date:** October 25th, 2023

**DOI:** <https://doi.org/10.21203/rs.3.rs-3403392/v1>

**License:**  This work is licensed under a Creative Commons Attribution 4.0 International License. [Read Full License](#)

---

**Version of Record:** A version of this preprint was published at Environmental Science and Pollution Research on December 14th, 2023. See the published version at <https://doi.org/10.1007/s11356-023-31453-0>.

# Abstract

The current investigation concerns with preparation eco-friendly and cost-effective adsorbent (mesoporous silica nanoparticles (Mes-Si-NPs)) based on black liquor (BL) containing lignin derived from sugarcane bagasse and combining it with sodium silicate derived from blast furnace slag (BFS) for thorium adsorption. Thorium ions were adsorbed from an aqueous solution using the synthesized bio-sorbent (SBL), which was then assessed by X-ray diffraction, BET surface area analysis, scanning electron microscopy with energy dispersive X-ray spectroscopy (EDX) and Fourier transforms infrared spectroscopy (FTIR). Th(IV) sorption properties, including the pH effect, uptake rate and sorption isotherms across various temperatures were investigated. The maximum sorption capacity of Th(IV) on SBL is 158.88 mg/L at pH value of 4, 328 K, and 60 min contact time. We demonstrated that the adsorption processes comport well with pseudo-second-order and Langmuir adsorption models considering the kinetics and equilibrium data. According to thermodynamic inspections results, the Th(IV) adsorption process exhibited endothermic and random behavior suggested by positive  $\Delta H^\circ$  and  $\Delta S^\circ$  values, while the negative  $\Delta G^\circ$  values indicated a spontaneous sorption process. The maximum Th(IV) desorption from the loaded SBL (Th/SBL) was carried out at 0.25 M of  $\text{NaHCO}_3$  and 60 min of contact. Sorption/desorption processes have five successive cycles. Finally, this study suggests that the recycling of BFS and BL can be exploited for the procurement of a promising Th(IV) adsorbents.

## 1. Introduction

Thorium (Th(IV)) has low radioactivity, occurs naturally and widely distributed over the earth's crust, making it roughly three times as plentiful as uranium (Liu et al. 2014) (Mastren et al. 2018) (Mastren et al. 2017). Th(IV) has widespread application in an extensive palette of disciplines, including radios, optics, aerospace, chemistry, metallurgy, nuclear industry, nuclear medicine and materials research, giving it both scientific and economic significance. The accumulation of massive amounts of trash around the world has exacerbated the pollution crisis, as this garbage has the aptitude to ascend the food chain and be consumed by human beings, where it can cause long-term harm to vital organs and even death (Baybaş & Ulusoy 2011) (Keshtkar & Hassani 2014). Harmful Th(IV) pollution is significant because it bioaccumulates in human tissues via the food chain. After being exposed to Th(IV), human liver cells proliferated at a rate that was 40–60% higher than usual (Rezk 2018). Consequently, the separation and recovery of Th(IV) from radioactive wastewater has substantial scientific and practical importance.

Precipitation (Hamed et al. 2016), solvent extraction, membrane separation (Li et al. 2018), ion exchange (Ang et al. 2018), and adsorption (Ding et al. 2019b) (Varala et al. 2019) are just a few of the methods developed recently for Th(IV) extraction, preconcentration, and separation from wastewater. Chemisorption systems are the most ubiquitous method for Th(IV) elimination from fluids because they are simple and straightforward technologies with a convenient process, increased practicability, pricing, and prospective removal routine (Xiong et al. 2017). The luckiness of this layout improves the efficiency with which the extraction is accomplished. This means that a line-up consisting of silica nanoparticles (Gomez et al. 2018), natural polymers, and magnetically sorptive materials (Atta & Akl 2015) (Wu et al. 2013) are ready to capture Th(IV) with the required level of efficiency. However, many of these materials suffer from flaws that limit their effective enforcement in environmental therapies, such as poor selectivity Th(IV) adsorption and limited chemical stability in powerful alkaline and acidic conditions. Consequently, designing a high-efficiency sorbent for thorium removal that has the right sorption capacity, exceptional selectivity, and pH is an exciting task.

To that end, the scientists' focus has been dragged toward waste management in an effort to preserve the planet. Waste management strategies include source reduction, proper disposal, and pollution elimination or mitigation (Ding et al. 2019a). Adsorption methods are first developed for Th(IV) recovery to extract radioactive components from liquid waste (Kaynar et al. 2021). A wide variety of sorbents have been used to purge radioactive elements from wastewater, including activated carbon (Omar & Moloukhia 2008), algae (Kim et al. 2019), modified nanoparticles (Xia et al. 2020), zeolites (Jiménez-Reyes et al. 2021), imprinted mesoporous silica (Yang et al. 2017), and so on. As a result of their wide availability, low cost, and low impact on the environment, adsorbents made from biomass waste have also attracted a lot of interest (Khosravi et al. 2022). The bagasse from sugarcane production is a type of agricultural waste that could be processed into silica. It's been asserted that natural silica is entirely harmless to handle and inexpensive and easy to produce with readily available materials. Using waste biomass to create mesoporous  $\text{SiO}_2$  for removing contaminants from aqueous solutions aids in both preserving an eco-friendly environment and repurposing waste streams to treat additional waste streams (Rahman et al. 2015).

Meanwhile, mesoporous bio-silica, an inorganic substance consisting of Si and oxygen, has gained a lot of interest since it is safe to use, stable, biocompatible, and easy to produce (Niculescu 2020). Mesoporous materials, i.e., porous materials with pore size at 2–50 nm, have garnered significant interest in a wide range of scientific disciplines over the past two decades (Boissiere et al. 2011) (Kwon et al. 2010) (Liang et al. 2006) (Liu et al. 2011) (Ma et al. 2011) (Yang et al. 2011). These substances were used to purge waste solutions of Th(IV). Moreover, mesoporous silica nanomaterials are unique families of attractive porous silica featuring very large specific surface areas, mechanical and thermal durability, extremely consistent pore arrangement, strong sorption capacity, and extraordinarily wide prospects of functionalization (Thirumavalavan et al. 2011) (Walcarius & Mercier 2010) (Yousefi et al. 2009). Because of these benefits, mesoporous silica is a great substrate for thorium extraction from geological and environmental samples. Solid-phase extraction has been reported to be used for Th(IV) recovery and preconcentration (Ghasemi & Zolfonoun 2010) (Jiang et al. 2019) (Lin et al. 2010). Mesoporous molecular screens (Al-MCM-41) were investigated for their ability to adsorb Th(IV). According to the findings, Th(IV) sorption on Al-MCM-41 was an endothermic and spontaneous process that reached equilibrium in 12 hrs (Zuo et al. 2011). Correspondingly, the produced nanoporous ZnO was used to remove Th(IV) from waste solutions, whereas nano tin oxide was used to remove Th(IV) and U(VI) ions from water (Kaynar et al. 2015) (Nilchi et al. 2013).

This investigation intended to prepare mesoporous silica nanoparticles (Mes-Si-NPs) using sugarcane bagasse-produced lignin with sodium silicate. This technique provides improved Mes-Si-NPs with pores and inner cavities for Th(IV) uptake from its solution. Also, Mes-Si-NPs was utilized for assessing the best sorption parameters of Th(IV) using the batch adsorption technique. Also, the isotherms and kinetics studies are studied for Th(IV) sorption on the synthesized Mes-Si-NPs.

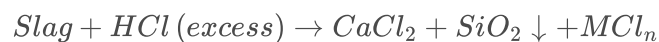
## 2. Materials and methods

### 2.1. Materials

Fluka AG in Switzerland was the source of the 36.5% hydrochloric acid, 98.0% ascorbic acid, 99.0% tartaric acid, and 99.0% Thoron. None of the precursor or reagents used in this work have undergone any extra purification procedures.; they were all of the analytical grades. The blast furnace slag (BFS) purchased from Helwan Company for Iron/ steel production (Helwan, Egypt). Sugarcane bagasse black liquor (BL) was gathered from the Qous company for paper industry (Qena, Egypt). To prepare a Th(IV) stock solution of 1000 mg/L, we dissolved 0.2535 g ( $\text{Th}(\text{NO}_3)_4 \cdot 6\text{H}_2\text{O}$ ) from Sigma-Aldrich into 100 mL of acidified de-ionized water (DW) with 10 mL of 36.5% HCl.

### 2.2. Extraction of $\text{Na}_2\text{SiO}_3$ from Blast Furnace Slag (BFS):

Granulated blast furnace slag (GBFS) was grinded, and sieved only to grains with particle size of  $> 50 \mu\text{m}$  (Amdeha et al. 2021). The chemical composition of BFS utilized in this study's is presented in Table S1. GBFS was treated with excess hydrochloric acid (3M) to elute metal components as expressed in the following equation:



Filtered solution contains  $\text{CaCl}_2$  and other metal chlorides ( $\text{M Cl}_n$  with  $\text{M} = \text{Al, Mg, Fe, Mn, etc.}$ ). Silica was filtrated out in gel form since it is not soluble in acid. After numerous rounds of washing with de-ionized  $\text{H}_2\text{O}$  and  $\text{C}_2\text{H}_5\text{OH}$  to remove any remaining acid, silica gel was dried at  $120^\circ\text{C}$  overnight. The obtained silica used as precursor of sodium silicate for preparation of Mes-Si-NPs adsorbents. Where the silica was then dissolved in a 5 M NaOH solution at  $90^\circ\text{C}$  for 2h, according to the following equation:



### 2.3. Black liquor-containing Lignin Extraction

Black liquor (BL) containing lignin is produced as a waste of paper and pulping process (El-Nemr et al. 2020) (Jonglertjunya et al. 2014). Firstly, spent sugarcane bagasse was sieved through a 60-mesh screen after drying at  $70^\circ\text{C}$  in electrical furnace overnight and milling for 3h. The subsequent processes gained the black fluid. 30 g of sugarcane bagasse powder were placed within a polytetrafluoroethylene-lined (PTFE-lined), 400 mL hydrothermal autoclave. The autoclave was filled with 240 mL of 5M NaOH and heated to  $150^\circ\text{C}$  for 3 hrs to facilitate a hydrothermal reaction. Allowing the autoclave to reach room temperature before filtration leads to almost complete separation of cellulose from the black liquor is in the form of a solid precipitate (Fig. S1). Lignin content in

black liquor is  $\approx 6.6$  g according to NREL (National Renewable Energy Laboratory) analytical technique ( $\approx 22\%$  lignin from sugarcane bagasse waste).

## 2.4. Mesoporous silica nanoparticles (Mes-Si-NPs) preparation

Sol-gel technology was used to make mesoporous silica particles (Zhu et al. 2017). For one hr, 30 g of sodium silicate ( $\text{Na}_2\text{SiO}_3$ ) were added to a BL containing lignin, and the mixture was agitated constantly at a  $\text{pH} \approx 13$ . The solution was then acidified with 3M  $\text{H}_2\text{SO}_4$  to precipitate lignin and  $\text{SiO}_2$  together (The initial  $\text{pH}$  of BL was 12–13 while the final  $\text{pH}$  of BL was adjusted to  $\text{pH} \approx 7$ ). The resulting colloidal precipitating reagent in the solution is a lignin/silica composite. The precipitate was centrifuged separately after an hour at  $70^\circ\text{C}$ . The precipitate was purified by washing several times with DW to remove any remaining contaminants before the lignin/silica composite was collected. To remove any remaining organic matter, the composite was calcined for 3 hrs at  $700^\circ\text{C}$  in air furnace; the resulting white product is Mes-Si-NPs (Fig. S1).

## 2.5. Characterization

Thorium contents in the original and removed samples measured by UV-vis spectrophotometer (Metertech Inc., model SP-8001, Taiwan) (Marczenko & Balcerzak 2000). mesoporous silica's crystal structure was studied with a Philips PW1390 X-ray diffractometer. Dynamic light scattering measurements with a Zetasizer Nano ZS was used to calculate the sorbent's zeta-potential (Malvern Instruments Ltd., Malvern, UK). Using a Quanta Chrome Nova 3200 analyzer,  $\text{N}_2$  adsorption/desorption isotherms at 77 K were examined to evaluate the textural properties of Mes-Si-NPs. Using a Nicolet Nexus-870 FTIR spectrometer (USA), The functional groups of the materials under study was investigated using Fourier transform infrared (FTIR) spectroscopy. The elemental composition and interaction mechanism of SBL adsorbent before and after adsorption was carried out using X-ray photoelectron spectroscopy (Thermo Fisher Scientific; USA). Physical morphology of sorbent beads was assessed by Scanning Electron Microscopy (SEM) while the chemical composition of SBL before and after thorium adsorption was investigated with Energy Dispersive X-ray spectroscopy (EDX).

## 2.6. Adsorption studies

In adequate glass beakers, 0.1 g of silica bio-adsorbent (SBL) was incorporated with 200 mL of Th(IV) working synthetic solutions whose concentrations range 50–400 mg/L at various temperatures to conduct targeted adsorption studies. At 200 rpm, the prepared mixtures were stirred using mechanical stirrer. 20 mL of sample solution is repeatedly removed at specified intervals and in  $\text{pH}$  ranging of 1–7. The used SBL adsorbent was filtered after each experiment to remove any tiny particles before being examined for the adsorbed metal ions. Multiple experiments are used to determine the desired levels of significant variables that affect the adsorption process, including  $\text{pH}$ , contact time, dose amount, initial Th(IV) concentration, and solution temperature. The mean value was always implemented in studies, which were all done in triplicate. whereas the analogous experiments are carried out to determine the Th(IV) equilibrium isotherm via mixing 0.1 g of SBL adsorbent with 200 mL of a different Th(IV) solution concentration at a temperature range of 298–328 K. In these studies, the mixture is agitated to equilibrium for a contact time of up to 3 hours. The following equation was used to determine how much Th(IV) was absorbed by the SBL adsorbent (mg/L):

$$q_e = (C_0 - C_e) \frac{V}{m}$$

Where  $q_e$  is the metal uptake (mg/g),  $C_0$  and  $C_e$  are the initial and equilibrium (mg/L) Th(IV) concentrations in the solution, respectively, solution volume (L) expressed by  $V$  and  $m$  is the mass (g) of the SBL adsorbent.

## 2.7. Desorption and reusability studies

The loaded SBL adsorbent from the previous adsorption step was subjected to desorption in order to evaluate the desorption characteristics of Th(IV).  $\text{NaHCO}_3$  is used as an eluent for metal-loaded sorbent. Each desorption run is achieved by shaking 0.2 g of SBL adsorbent saturated by Th(IV) with 20 mL of 0.25 M  $\text{NaHCO}_3$  for 1 hr at  $25^\circ\text{C}$  and shaking speed 200 rpm. After filtering Thoron is used to measure Th(IV) concentration spectrophotometrically in filtrate. The following equations were used for estimating the regeneration quantity ( $RE$ ) and desorption efficacy ( $DE$ ):

$$DE = \left( \frac{C_D \times V}{q_d \times m} \right) \times 100$$

$$RE = \frac{q_d}{q_e} \times 100$$

Where  $q_d$  (mg/g) is the sorption capacity for metal-loaded material (before desorption experiment) and  $q_e$  (mg/g) is the sorption capacity at the first cycle,  $C_D$  (mg/L) is the Th(IV) concentration in the eluate. Between each sorption and desorption cycle, demineralized water was used for rinsing.

Between each sorption and desorption cycle, demineralized water was used for rinsing. Th(IV) sorption and desorption efficiencies were evaluated through five successive sorption-desorption cycles using the same sorbent in order to evaluate the reusability of the sorbent. According to the experimental sorption conditions, 400 mL of a 50 mg/L Th(IV) solution and 0.2 g of sorbent must be mixed for 60 min before metal analysis and a mass balance calculation are performed. Then the desorption step cycled as reported above. The value obtained for the first cycle was compared to the sorption efficiency after five regeneration cycles.

## 3. Results and discussion

### 3.1. Sorbent description

#### 3.1.1. XRD analysis

XRD pattern of the mesoporous-SBL adsorbent was illustrated in Fig. 1. The diffraction spectrum of mesoporous-SBL exhibited a major broad peak at  $2\theta = 24^\circ$ . Due to crystalline silica not forming at a low calcined temperature (700 °C), the large diffused peak indicated that only amorphous silica had formed (Proctor et al. 1995). On the other hand, silica starts to crystallize above 900 °C, and the calcination temperature has a significant impact on this process (Bakar et al. 2016).

#### 3.1.2. BET and BJH analysis

Textural features of the Mes-Si-NPs sorbent were examined using BET measurements (Fig. 2). According to the Langmuir classification, the sorption and desorption patterns might be categorized as H1-type isotherms. The isotherm showed a hysteresis loop characteristic. A long extended cylindrical pore type is a characteristic of this type of isotherm. The surface area (Brunauer-Emmett-Teller, or BET analysis), pore volume (Barrett, Joyner, and Halenda, or BJH analysis), and average pore diameter were determined using the N<sub>2</sub> adsorption isotherm method. Specific surface area ( $SSA_{BET}$ ) of mesoporous SBL was found to be 42.96 m<sup>2</sup>/g with an average pore diameter of  $\approx 1.5$  nm (i.e., the pore size distribution profile showed a monomodal class). Moreover, the pore volume of 0.074 cm<sup>3</sup>/g.

#### 3.1.3. SEM & EDX Studies

The most dependable and practical method for assessing the physical morphology of sorbent beads is SEM. In addition, as shown in Fig. 3a,b mesoporous SBLs surface and physical structures were examined using SEM. It displayed different compositions and structures, as well as distinct roughness. The mesoporous SBL skeleton was built from various unrelated pieces with varying diameters. In addition, the photograph taken after the SBL was uptake with Th(IV) shows that the figure was constructed from aggregate particles with bigger interstitial holes.

Chemical composition of SBL before and after thorium adsorption was investigated with EDX, as shown in Fig. 3c,d. Before adsorption, the chemical constitution of SBL was discovered. Only Si (31.81%) and O (68.19%) peaks were noticeable from the data in Fig. 3c; no other peaks were found. The only silica structures that contain SiO<sub>4</sub> tetrahedra have an approximate 1:2 silicon to oxygen atomic ratio, and the 1:2 ratio of SBL demands that two tetrahedra share each oxygen atom in silica (Douglas & Ho 2006). It indicates that the prepared SBL is highly pure. After Th(IV) adsorption on the adsorbent, the chemical composition change Fig. 3d that there was a distinct peak of Th(IV) on the adsorbent spectrum. Th(IV) adsorption on SBL was confirmed by the occurrence of a Th(IV) peak.

#### 3.1.4. FTIR analysis

FTIR spectroscopy was implemented for studying SBL and Th/SBL, and the results are shown in Fig. 4. In the SBL spectrum, a prominent peak at about  $1103\text{ cm}^{-1}$  is observed, which is the stretching Si-O asymmetric vibrational band (Das & Das 2015). The peak at  $823\text{ cm}^{-1}$  is Si-O, the symmetric bending vibration owing to the motion of oxygen atoms (Moncada et al. 2007). The peak at  $505\text{ cm}^{-1}$  is Si-O-Si bending vibration (Thambiliyagodage et al. 2020). The broad peak at around  $3375\text{ cm}^{-1}$  was contributed to the O-H stretching vibration band. The peak at  $2350\text{ cm}^{-1}$  can be originated from absorbed water (Qasim et al. 2015). FTIR spectrum of the prepared silica after calculations suggested that prepared SBL is pure and free from organic matter.

After Th(IV) adsorption, as shown in Fig. 4 (Th/SBL spectrum), the -OH vibration band for the sorbent was reduced to  $3369\text{ cm}^{-1}$ , which could be caused by the linkage of Th(IV) to the SBL surfaces. Additionally, intense peaks were identified at  $1381\text{ cm}^{-1}$  for Th/SBL; this peak matched to the Th-O vibration band of Th(IV), demonstrated that Th(IV) adsorption on the SBL adsorbent occurred. (Pool et al. 2005). Also, other peaks that appeared at 630, 580, and  $550\text{ cm}^{-1}$  give a good evidence for adsorption of Th(IV) on the SBL adsorbent surfaces.

### 3.1.5. XPS analysis

X-ray photoelectron spectroscopy (XPS) is one of the most popular spectroscopic techniques because of its capability to differentiate among the various chemical states employing experimentally determined chemical shifts. The chemical compositions of SBL sorbent and its complexation with Th(IV) were investigated by XPS (Fig. 5a). XPS spectra of prepared sorbent showed C  $1s$  (287.22–290.35 eV), O  $1s$  (534.20–536.68 eV) (Jensen et al. 2013), Si  $2p$  (105.13–109.14 eV), signal obtained before and after Th(IV) complexation. Unexpectedly, the detection of two signals at 534 eV and 105 eV, respectively, that together constitute the O  $1s$  and Si  $2p$  signals, demonstrates that the sorbent contains silicon and oxygen components. The absorbed Si  $2p$  signal at 105.13 eV reveals the existence of pure SBL (Jensen et al. 2013) (Kanungo et al. 2010) (Pal et al. 2014).

The O  $1s$  spectral signal peak absorbed at 534.2 eV clearly shows increased oxygen contribution with porous silica (Jensen et al. 2013) (Pal et al. 2014). Table S2 shows the binding energies (BEs, eV) and atomic fractions (%) of SBL and Th/SBL. The XPS atomic analysis of SBL exhibits the ratio Si (27.98%) / O (59.78%) is 2.13, whereas the SBL stoichiometric ratio is 2.0. Figure 5a and Table S2 summarize the XPS survey scan spectra of mesoporous SBL and the deconvoluted bands of Na  $1s$ , Cl  $2p$ , Si  $2p$ , C  $1s$ , and O  $1s$ , signals (from High-resolution (HRES) XPS spectra). According to survey scans, the substance is mainly silicon and oxygen with tiny contamination from carbon, sodium, and chlorine.

Meanwhile the Si  $2p$  spectrum is deconvoluted, it reveals two primary components that correspond to a Si-C bond at 101.08 eV and a Si-O/Si-O-C bond (silicon oxide/silicon oxycarbide) at 102.08 eV, respectively. The oxycarbide phases may have grown on the film's surface as due to of prolonged contact with environment. (Avila et al. 2000) (George et al. 2002). For Si  $2p$  spectra in Fig. 5a, only one chemical structure corresponding to the Si oxidation state Si(IV) was clearly observed at a binding energy of 105.13 eV (Campbell et al. 2009) (Rellergert et al. 2010).

The thorium sorption on SBL is confirmed by the incidence of Th  $4f$  peaks at 339.86 eV. The distinctive doublets of Th  $4f_{5/2}$  and Th  $4f_{7/2}$  are depicted at 344.82 and 335.45 eV in Fig. 5b, providing strong evidence that Th/SBL formed. (Hu et al. 2022) (Liu et al. 2022). Notably, a small amount of chloride (Cl  $2p$ ) is presented in both spectra (SBL and Th/SBL); it may be due to the usage of DW during the sorbent preparation.

## 3.2. Thorium sorption properties

### 3.2.1. Effect of pH

The sorption of thorium species by a particular sorbent is significantly influenced by the pH. The Th(IV) adsorption uptake for the mesoporous SBL was measured for the pH range of pH (1–7) at room temperature, 200 mL of 50 mg/L Th(IV), and 0.1 g porous SBL dose, for 3 hrs contact time (Fig. 6a). From the data, at pH < 3, Th(IV) adsorption capacity on porous SBL gradually decreased to a low value. The reduced rate of Th(IV) adsorption is reasonably understood in the light of competence between the hydrolyzed thorium species (Th(IV),  $\text{Th}(\text{OH})_2^{2+}$  and  $\text{Th}(\text{OH})^{3+}$ ) on the mesoporous SBL binding sites as well as the increased solubility of the thorium species (Kaynar et al. 2023). At pH > 3, the negative surface charges on the porous SBL start to increase, and Th(IV) uptake

capacity increased due to the increase of the attraction between the thorium cationic species and porous SBL. Due to the fact that Th(IV) were initially precipitated at pH > 4 in accordance with the species distribution for Th(IV) hydrolysis, the capacity of thorium ions to bind to mesoporous SBL declined as pH increased > 4 (Ding et al. 2019c).

Moreover, Zeta potential and pH effect were examined to pH values 8 in the desired system. As shown in Fig. 6b, the zeta potential corresponding to the pH of SBL sorbent was determined at 2 to 8 with a surface charge between + 6 mV to - 42 mV. When the surface charge was decreased gradually till pH > 2.8, the negative charge of the sorbent surface was increased. Hence, the pH of the point of zero charges ( $pH_{pzc}$ ) was measured at 2.8. As the pH continued to decrease from  $pH_{pzc}$ , the surface charge remained slightly positive charge (< + 6 mV). Meanwhile, increasing the pH above  $pH \approx 2$  (Fig. 6a) affected the surface charge (Zeta potential) and negative charge increase to - 42 mV. The porous SBL had a negative charge; in the interim, the pH persisted larger than the  $pH_{pzc}$  that might be appropriate for Th(IV) adsorption; this indicated that the surfaces would be negatively charged and functionalized with Si-O, which is beneficial for the sorption of thorium ions due to electrostatic attraction and chemical sorption. Consequently, the best sorption pH for Th(IV) is 4.

### 3.2.2. Contact time impact and kinetics

The Th(IV) adsorption is shown as a function of time in Fig. 7a. The contact duration between the Th(IV) solution and the solid sorbent is crucial to the Th(IV) adsorption reaction because it may reveal the kinetics of interactions between the surface sorbent and Th(IV). For this purpose, contact time effect on Th(IV) adsorption onto Mes-Si-NPs was investigated at 50 mg/L Th(IV), pH  $\approx$  4, and 0.01 g sorbent. The uptake of Th(IV) ions reached about 64.25 mg/g of the uptake plateau within 30 min. The abundance of active sites on the adsorbent surface may be the cause of the initial promptly adsorption. There are three kinetic characteristics steps, which can be summed up as follows:

Due to the significant initial concentration difference between the solution and the surface-active sites, the accessible external sites initially exhibit rapid initial sorption and a nearly linear increase in sorption capacity with time. Mainly, in the first 30 min, about 64.25 mg/g of the total sorption of the sorbent. Secondly, slowly increase with increasing sorption time (till 30–60 min), representing more than 92.0 mg/g of total sorption associated with a decrease in the concentration gradient and mesoporous in the polymer network. Lastly, for the adsorbent, the adsorption capabilities were fixed after 60 min, whilst the further time increment had no effect on the adsorption of Th(IV). Therefore, the equilibrium experiments require 60 min of contact time. The resulting adsorption/time data were fitted using the simplified intraparticle diffusion equations (sIPDE) kinetics, simplified pseudo-second-order linear equations (sPSOLE), and simplified pseudo-first-order equations (sPFOLE) (Weber and Morris) (Sen et al. 2017). Figure 7b-d describes the kinetic profiles for the sPFOLE, sPSOLE and sIPDE using the kinetic linear equations for the three models and model parameters summarized in Table S3. The performance of the straight line ( $R^2$ ) was utilized to evaluate each model's validity, which was higher in sPSOLE than those of sPFOLE and sIPDE, as well as the consistency between experimental and calculated values of  $q_e$ ; the sorption capacity ( $q_{e,cal}$ ) was closer to the experimental sorption capacity ( $q_{e,exp}$ ) for the sPSOLE. So, the data revealed that the sPSOLE model was ideal for describing the sorption. As shown in Fig. 7b,c and Table 1, the adsorption data suggested that the rate-limiting adsorption step followed the pseudo-second-order model.

The adsorption process would be governed by intraparticle diffusion; in contrast, the regression of  $q_t$  vs  $t^{0.5}$  in the intraparticle diffusion model is linear and passes through the origin. The positive values of C show that intraparticle diffusion was not the only rate-controlling step, as shown by  $R^2$  of 0.925 in Fig. 7d (Sen et al. 2017). These results reveal that the sPSOLE was an ideal model for describing the sorption process. A chemisorption reaction involving valence forces for sharing or exchanging electrons through complexation between the sorbent surface and metal ions is suggested to have taken place during the sorption of Th(IV).

Table 1  
Kinetics parameters for Th(IV) sorption on mesoporous SBL

sPFOLE			sPSOLE			sIPDE		
$k_1$	$q_e$	$R^2$	$k_2$	$q_e$	$R^2$	C	$k_{int}$	$R^2$
0.0624	111.17	0.907	$7.9 \times 10^{-4}$	102.04	0.997	2.06	11.742	0.925

### 3.2.3. Sorption isotherms

Th(IV) ion adsorption isotherm on the examined sorbent at different Th(IV) concentrations (50–400 mg/L), pH  $\approx$  4, 1 hr contact time, and different temperatures (298–328 K) are shown in Fig. 8a. Sorption isotherms illustrated whereby Th(IV) combined with Mes-Si-NPs, and it provided the required essential materials for the strategy of the Th(IV) adsorption system. They describe the relationship between the equilibrium Th(IV) concentration in the solution ( $C_e$ ) and the amount of Th(IV) adsorbed onto the sorbent ( $q_e$ ) at a fixed temperature. Utilizing the linear versions of the Langmuir, Freundlich, and Temkin equations, the sorption processes were examined (Ding et al. 2019c). Table S4 reports and expresses the linear forms of the Langmuir, Freundlich, and Temkin equations. The fitting of experimental profiles using the Langmuir, Freundlich, and Temkin equations is shown in Fig. 8b,c,d.

The uptake of Th(IV) ions went up with increase Th(IV) concentration and also increased with rising temperature as the initial and equilibrium concentrations regularly increased, according to the adsorption curves at different temperatures. As the driving force elevates, enough energy is generated between solution and the active sorption site (Fig. 8a). The maximum uptake of SBL toward Th(IV) was found to be 158.88 mg/g at 328 K.

Langmuir, Freundlich, and Temkin models are plotted in Fig. 8, and their relevant parameters are reported in Table 2. The uptakes ( $q_e$ ) for Langmuir (104.16, 117.65, 135.14, 151.52 mg/g) at 298, 308, 318, 328 K were nearer to the experimental uptakes ( $q_{e,exp}$ ), which are 106.33, 122.03, 143.70, and 158.88 mg/g, respectively. Moreover,  $R^2$  for the Langmuir generally has higher coefficients than the Freundlich and Temkin coefficients, regardless of sorbent type and temperatures. These findings indicated that SBL was homogenous in solutions, and the Th(IV) sorption technique followed the Langmuir isotherm. Additionally, it argues that a finite number of identical sites are dispersed over the sorbent surface and that metal sorption occurs through monolayer uniform sorption. Additionally, the Langmuir constant values ( $b$ ) related to the sorption energy greater than 0.05 L/mg indicate that the higher force between the sorbent and the adsorbate results from chemical interaction (Araújo et al. 2018) (Rangabhashiyam et al. 2014). These results indicate that the sorption is favorable at a high temperature (i.e., increasing interaction of reactive groups with Th(IV)), hence it is anticipated that the sorption will be endothermic.

Temkin isotherm proposes the assumption that the surface covering affects the sorption's free energy. The constant  $A_T$  reflects the initial sorption heat for the sorbent; the  $A_T$  values are decreased with increasing the temperatures to 328 K. Hence the lower affinity of the sorbent to the sorbate (Araújo et al. 2018) (Rangabhashiyam et al. 2014). Furthermore,  $R^2$  values are the smallest when compared with the  $R^2$  of Langmuir and Freundlich models. The data showed that the Temkin model did not fit the experimental data. The obtained data illustrates that sorption processes are fitted well with the Langmuir isotherm model.

Table 2  
Th(IV) sorption isotherm parameters for Langmuir, Freundlich and Temkin equations

Temp. (K)	$q_{exp}$ (mg/g)	Langmuir isotherm			Freundlich isotherm			Temkin isotherm			
		$q_{max}$ (mg/g)	$b$ (L/mg)	$R^2$	$n$	$k_F$ (mg/g)	$R^2$	$A_T$ (J/mol)	$K_T$ (L/mg)	$b_T$	$R^2$
298	106.33	104.16	0.158	0.996	2.98	24.77	0.985	19.98	1.75	1.24	0.933
308	122.03	117.65	0.171	0.994	2.89	27.35	0.995	23.19	1.65	110	0.958
318	143.70	135.14	0.185	0.993	3.74	41.62	0.976	21.86	1.52	121	0.923
328	158.88	151.52	0.194	0.993	3.42	43.87	0.988	25.27	1.44	108	0.932

### 3.2.4. Temperature impact and sorption thermodynamic

The temperature impact was assessed for Th(IV) sorption at different sorption temperatures (298, 308, 318 and 323 K). The maximal sorption capacity increases with increasing temperature, as seen in Fig. 8a. Hence, the sorption process is endothermic for each temperature. The thermodynamic equilibrium constant,  $K_d$ , for the sorption is determined from the experimental data. The Van't Hoff equations is used to study the thermodynamic parameters (enthalpy change ( $\Delta H^\circ$ ), entropy change ( $\Delta S^\circ$ ), free energy change ( $\Delta G^\circ$ ), as follow:



$$K_d = \frac{q_e}{C_e}$$

$$\ln K_d = \frac{\Delta S}{R} - \frac{\Delta H}{RT}$$

$$\Delta G = \Delta H - T\Delta S$$

Figure S2 illustrate the linear curve of  $\ln K_d$  vs.  $1/T$ . A good fit of experimental data is obtained and permits the determination of thermodynamic parameters of Mes-Si-NPs sorbent in Table 3.  $\Delta H^\circ$  value is + 28.39 kJ/mol, which confirms the endothermic nature of the sorption process, and the reaction becomes more favorable at high temperatures. The entropy change is + 0.209 kJ/mol, which indicates an increase in randomness after Th(IV) sorption at the solid/liquid interface and the feasibility of adsorption. Also,  $\Delta G^\circ$  values range from - 33.89 to - 40.16 kJ/mol, indicating the spontaneous sorption reaction. The  $-\Delta G^\circ$  values increased with increasing temperature, confirming that the sorption spontaneity increased.

Table 4 investigates and contrasts the sorption characteristics of Th(IV) for various sorbents. It is challenging to make a direct comparison considering the experimental conditions (such as sorbent dosage, duration, pH, and solution composition) are not the same. However, the maximum sorption capacities of the comparing adsorbents are in the term uptakes ( $q_{max}$ ) among the most efficient Th(IV) recovery from acidic solutions (at pH  $\approx$  4). This is shown that mesoporous SBL has a good sorption activity with the advantages of a low-cost and facile synthetic method.

Table 3  
Thermodynamic parameters of Th(IV) sorption by SBL sorbent

Temp. (K)	$\Delta H^\circ$ (kJ/mol)	$\Delta S^\circ$ (kJ/mol K)	$\Delta G^\circ$ (kJ/mol)	T $\Delta S^\circ$ (kJ/mol)	R <sup>2</sup>
298	28.39	0.209	-33.89	62.28	0.974
308			-38.98	64.37	
318			-38.07	66.46	
328			-40.16	68.55	

Table 4  
Maximum sorption capacity for Th(IV) ions with selected sorbents

Adsorbent	Uptake (mg/g)	Ref.
Organophosphate polymer	27.84	Luca & Hanna 2015
Modified mesoporous silica	49.00	Yousefi et al. 2009
Activated carbon	20.18	Kütahyalı & Eral 2010
PVA/Fe <sub>3</sub> O <sub>4</sub> /SiO <sub>2</sub> composite	62.50	Mirzabe & Keshtkar 2015
Humic acid	4.64	Khalili & Al-Banna 2015
N,N,N',N'-tetraoctyldiglycolamide impregnated graphene aerogel	66.80	Chen et al. 2018
Triethylene-tetramine modified magnetic chitosan	133.30	Xu et al. 2015
Mesoporous silica nanoparticles (Mes-Si-NPs)	158.88	Present study

### 3.3. Th(IV) desorption and SBL sorbent recycling

Figure 9 and Table S5 illustrate the efficiency of SBL adsorbent for Th(IV) adsorption and desorption for 5 cycles. A crucial phase in the design of a sorption system is the metal desorption step. Indeed, this is most beneficial in improving the target metal concentration for the ultimate recovery or removal of Th(IV). Furthermore, experiments for sorbent regeneration should be done in order to attain a sorption of lowest expenses. So, desorption studies were conducted aimed to assess the eluting performance of the

sorbent and its regeneration. Preliminary studies revealed that 20 mL of 0.25 M NaHCO<sub>3</sub> solution efficiently desorbed Th(IV) (96.04% desorption in the first cycle) from 0.2 g of Th/SBL at 60 min desorption equilibrium time, as shown in Fig. 9.

A reusability experiment was used to evaluate the regeneration-reuse feature. The adsorption-desorption study also was a critical factor in diminishing the recovery cost of Th(IV). Mesoporous SBL regeneration and reuse was examined. Figure 9 and Table S5 reported that Th(IV)'s sorption-desorption efficiency on mesoporous SBL decreased slowly with increasing cycle number. The regenerated and reused sorbent was washed with 50 mL DW to eliminate any entrained sodium ions regeneration solution from sorbent before recycling it into the Th(IV) sorption system. The sorption-desorption step was repeated five times. The desorption efficiency re-expanded up to 81.43% of the preliminary desorption efficiency. As a result, mesoporous SBL with long-term stability may be thought of a superb, reusable sorbent for Th(IV) recovery. It suggests an excellent performance with repeated usage in Th(IV) recovery from aqueous solutions. The sorbent has good durability/stability in terms of sorption capacity.

### 3.4. Mechanism of adsorption

At pH < 2.8, thorium species was mainly in the form of Th(IV) (Fig. S3), while SBL was positively charged due to the high protonation, as reported before in zeta potential interpretation. According to (Liao et al. 2022) Th(IV) and separating agents may exhibit considerable electrostatic attraction, leading to a low separation efficiency. Th(IV) could be bound by the active sites of the separating agent at pH > 2.8 owing to the strengthening of the electrostatic attraction between it and the Th(IV) due to the intensification of deprotonation with rising pH (Liu et al. 2021). The negatively charged sites of the SBL adsorbent have a high tendency to occupied by the positively thorium species (Th(IV), Th(OH)<sub>2</sub><sup>2+</sup> and Th(OH)<sub>3</sub><sup>3+</sup>), as showed in Fig. S3. According to of the significant pH dependence, our findings showed that surface complexation was the primary mechanism of SBL for Th(IV) separation (Zhao et al. 2021). The conversion of silica derived BFS and BL into mesoporous silica nanoparticles (Mes-Si-NPs) adsorbent for the separation and recovery of valuable metals would be expected to realize the waste management of industrial waste by-products.

## 4. Conclusion

Mesoporous silica nanoparticles (Mes-Si-NPs) were synthesized and fully characterized to produce an efficient bio-sorbent for Th(IV) recovery. FTIR analysis and zeta-potential measurements confirmed the expected structures of the studied material. To pinpoint its ideal sorption parameters, Th(IV) sorption experiments were conducted on the proposed bio-sorbent. As temperature increased from 298 to 328 K at a pH ≈ 4, upon adding 0.01 g of silica bio-adsorbent to 20 mL of 50 mg/L Th(IV) for an hour of contact time, the maximum sorption capacity rose from 106.33 to 158.88 mg/g. sPSOLE models effectively uptake kinetics while the sorption isotherm is compatible with the Langmuir model. The thermodynamic parameters were determined to show the endothermic and spontaneous sorption reaction. Besides, system randomness increases with Th(IV) sorption. Sodium bicarbonate solution (0.25 M) was utilized for the bio-sorbent effectively rejuvenation. Finally, mesoporous silica nanoparticles (Mes-Si-NPs) prepared from BFS and BL lignin presents a novel utilization of the two wastes.

## Declarations

### Declaration of competing interest

The authors declare that they have no known competing financial interests or personal relationships that could have appeared to influence the work reported in this paper.

### Data availability

Data will be made available on request.

### Funding

This work was funded by the Deanship of Scientific Research at Jouf University under Grant No (DSR2022-RG-0139).

### Ethical Approval

Not applicable

### Consent to Participate

Not applicable

### Consent to Publish

All authors agree to publish the manuscript in ESPR journal.

### Authors Contributions

Ahmed H. Naggat and Al-Sayed A. Bakr: supervised, conceptualization and organized this manuscript. Abdelghaffar Dhmees and Tarek A. Seaf-Elnasr: carried out the experimental data, performed the material characterizations and theoretical calculations. Hazim M. Ali, Rasmih M. Kh. Alshamery and Lubna H. M. AlNahwa: literature search, data curation and validation. Kwok F. Chong and Gomaa A.M. Ali: writing and revision the original draft. All authors contributed to the discussion and interpretation of the results obtained throughout work on the manuscript. All authors read, drafted and approved the manuscript final version for publication.

## References

1. Amdeha, E., Mohamed, R.S., Dhmees, A.S., 2021. Sonochemical assisted preparation of ZnS-ZnO/MCM-41 based on blast furnace slag and electric arc furnace dust for Cr (VI) photoreduction. *Ceram. Int.* 47, 23014–23027.
2. Ang, K.L., Li, D., Nikoloski, A.N., 2018. The effectiveness of ion exchange resins in separating uranium and thorium from rare earth elements in acidic aqueous sulfate media. Part 2. Chelating resins. *Miner. Eng.* 123, 8–15.
3. Araújo, C.S.T., Almeida, I.L.S., Rezende, H.C., Marcionilio, S.M.L.O., Léon, J.J.L., de Matos, T.N., 2018. Elucidation of mechanism involved in adsorption of Pb(II) onto lobeira fruit (*Solanum lycocarpum*) using Langmuir, Freundlich and Temkin isotherms. *Microchem. J.* 137, 348–354.
4. Atta, A.M., Akl, Z.F., 2015. Removal of thorium from water using modified magnetite nanoparticles capped with rosin amidoxime. *Mater. Chem. Phys.* 163, 253–261.
5. Avila, A., Montero, I., Galán, L., Ripalda, J.M., Levy, R., 2000. Behavior of oxygen doped SiC thin films: An X-ray photoelectron spectroscopy study. *J. Appl. Phys.* 89, 212–216.
6. Bakar, R.A., Yahya, R., Gan, S.N., 2016. Production of high purity amorphous silica from rice husk. *Procedia Chem.* 19, 189–195.
7. Baybaş, D., Ulusoy, U., 2011. The use of polyacrylamide-aluminosilicate composites for thorium adsorption. *Appl. Clay Sci.* 51, 138–146.
8. Boissiere, C., Grosso, D., Chaumonot, A., Nicole, L., Sanchez, C., 2011. Aerosol route to functional nanostructured inorganic and hybrid porous materials. *Adv. Mater.* 23, 599–623.
9. Campbell, C.J., Steele, A.V., Churchill, L.R., DePalatis, M.V., Naylor, D.E., Matsukevich, D.N., Kuzmich, A., Chapman, M.S., 2009. Multiply charged thorium crystals for nuclear laser spectroscopy. *Phys. Rev. Lett.* 102, 233004.
10. Chen, M., Li, Z., Geng, Y., Zhao, H., He, S., Li, Q., Zhang, L., 2018. Adsorption behavior of thorium on N,N,N',N'-tetraoctyldiglycolamide (TODGA) impregnated graphene aerogel. *Talanta* 181, 311–317.
11. Das, R.K., Das, M., 2015. Catalytic activity of acid and base with different concentration on sol-gel kinetics of silica by ultrasonic method. *Ultrason. Sonochem.* 26, 210–217.
12. Ding, H., Luo, X., Zhang, X., Yang, H., 2019a. Alginate-immobilized *Aspergillus niger*: Characterization and biosorption removal of thorium ions from radioactive wastewater. *Colloids Surf., A* 562, 186–195.
13. Ding, H., Luo, X., Zhang, X., Yang, H., 2019b. Efficient thorium removal by alginate-immobilized *Aspergillus niger*: characterization, kinetics, thermodynamic and mechanism analysis. *J. Radioanal. Nucl. Chem.* 319, 869–880.
14. Ding, H., Zhang, X., Yang, H., Luo, X., Lin, X., 2019c. Highly efficient extraction of thorium from aqueous solution by fungal mycelium-based microspheres fabricated via immobilization. *Chem. Eng. J.* 368, 37–50.
15. Douglas, B.E., Ho, S-M. 2006. Crystal Structures of Silica and Metal Silicates. In: *Structure and Chemistry of Crystalline Solids*. Springer, New York, pp. 233–278.

16. El-Nemr, K.F., Mohamed, H.R., Ali, M.A., Fathy, R.M., Dhmees, A.S. 2020. Polyvinyl alcohol/gelatin irradiated blends filled by lignin as green filler for antimicrobial packaging materials. *Int. J. Environ. Anal. Chem.* 100, 1578–1602.
17. George, V.C., Das, A., Roy, M., Dua, A.K., Raj, P., Zahn, D.R.T., 2002. Bias enhanced deposition of highly oriented  $\beta$ -SiC thin films using low pressure hot filament chemical vapour deposition technique. *Thin Solid Films* 419, 114–117.
18. Ghasemi, J.B., Zolfonoun, E., 2010. Simultaneous spectrophotometric determination of trace amounts of uranium, thorium, and zirconium using the partial least squares method after their preconcentration by  $\alpha$ -benzoin oxime modified Amberlite XAD-2000 resin. *Talanta* 80, 1191–11197.
19. Gomez, I.J., Arnaiz, B., Cacioppo, M., Arcudi, F., Prato, M., 2018. Nitrogen-doped carbon nanodots for bioimaging and delivery of paclitaxel. *J. Mater. Chem. B* 6, 5540–5548.
20. Hamed, M.M., Hilal, M.A., Borai, E.H., 2016. Chemical distribution of hazardous natural radionuclides during monazite mineral processing. *J. Environ. Radioact.* 162–163, 166–171.
21. Hu, Y., Ding, J., Ren, G., Jin, T., Liu, Z., Qian, Y., 2022. Highly efficient extraction of thorium from aqueous solution by 2-carboxyethylphosphonic acid-functionalized chitosan xerogel. *Sep. Purif. Technol.* 303, 122188.
22. Jensen, D.S., Kanyal, S.S., Madaan, N., Vail, M.A., Dadson, A.E., Engelhard, M.H., Linford, M.R., 2013. Silicon(100)/SiO<sub>2</sub> by XPS. *Surf. Sci. Spectra* 20, 36–42.
23. Jiang, Z., Xie, F., Kang, C., Wang, Y., Yuan, L., Wang, Y., 2019. Adsorption of thorium(IV) from aqueous solutions by poly(cyclotriphosphazene-co-4,4'-diaminodiphenyl ether) microspheres. *J. Radioanal. Nucl. Chem.* 321, 895–905.
24. Jiménez-Reyes, M., Almazán-Sánchez, P.T., Solache-Ríos, M., 2021. Radioactive waste treatments by using zeolites. A short review. *J. Environ. Radioact.* 233, 106610.
25. Jonglertjunya, W., Juntong, T., Pakkang, N., Srimarut, N., Sakdaronnarong, C., 2014. Properties of lignin extracted from sugarcane bagasse and its efficacy in maintaining postharvest quality of limes during storage. *LWT–Food Sci. Technol.* 57, 116–125.
26. Kanungo, J., Selegård, L., Vahlberg, C., Uvdal, K., Saha, H., Basu, S., 2010. XPS study of palladium sensitized nano porous silicon thin film. *Bull. Mater. Sci.* 33, 647–651.
27. Kaynar, Ü.H., Ayvackli, M., Hiçsönmez, Ü., Kaynar, S.Ç., 2015. Removal of thorium (IV) ions from aqueous solution by a novel nanoporous ZnO: Isotherms, kinetic and thermodynamic studies. *J. Environ. Radioact.* 150, 145–151.
28. Kaynar, Ü.H., Kaptanoglu, İ.G., Kaynar, S.Ç., Ugurlu, O., Yusan, S., Aytas, Ş., Madkhli, A.Y., Can, N., 2023. Adsorption of thorium (IV) ions using a novel borate-based nano material Ca<sub>3</sub>Y<sub>2</sub>B<sub>4</sub>O<sub>12</sub>: Application of response surface methodology and Artificial Neural Network. *Appl. Radiat. Isot.* 192, 110606.
29. Kaynar, Ü.H., Kaynar, S.Ç., Karali, E. E., Ayvackli, M., Can, N., 2021. Adsorption of thorium (IV) ions by metal ion doped ZnO nanomaterial prepared with combustion synthesis: Empirical modelling and process optimization by response surface methodology (RSM). *Appl. Radiat. Isot.* 178, 109955.
30. Keshtkar, A.R., Hassani, M.A., 2014. Biosorption of thorium from aqueous solution by Ca-pretreated brown algae *Cystoseira indica*. *Korean J. Chem. Eng.* 31, 289–295.
31. Khalili, F., Al-Banna, G., 2015. Adsorption of uranium(VI) and thorium(IV) by insolubilized humic acid from Ajloun soil–Jordan. *J. Environ. Radioact.* 146, 16–26.
32. Khosravi, A., Zheng, H., Liu, Q., Hashemi, M., Tang, Y., Xing, B., 2022. Production and characterization of hydrochars and their application in soil improvement and environmental remediation. *Chem. Eng. J.* 430, 133142.
33. Kim, I., Yang, H-M., Park, C.W., Yoon, I-H., Seo, B-K., Kim, E-K., Ryu, B-G., 2019. Removal of radioactive cesium from an aqueous solution via bioaccumulation by microalgae and magnetic separation. *Sci. Rep.* 9, 10149.
34. Kütahyalı, C., Eral, M., 2010. Sorption studies of uranium and thorium on activated carbon prepared from olive stones: Kinetic and thermodynamic aspects. *J. Nucl. Mater.* 396, 251–256.
35. Kwon, B.J., Ku, J.Y., Yu, K.H., Ko, J.E., Jung, H., 2010. Preparation and characterization of carbamoylphosphonate (CMPO) silane grafted on various mesoporous silicas. *J. Phys. Chem. Solids* 71, 663–668.
36. Li, F., Yang, Z., Weng, H., Chen, G., Lin, M., Zhao, C., 2018. High efficient separation of U(VI) and Th(IV) from rare earth elements in strong acidic solution by selective sorption on phenanthroline diamide functionalized graphene oxide. *Chem. Eng. J.* 332, 340–350.

37. Liang, Y., Hanzlik, M., Anwander, R., 2006. Periodic mesoporous organosilicas: mesophase control via binary surfactant mixtures. *J. Mater. Chem.* 16, 1238–1253.
38. Liao, J., Xiong, T., Zhao, Z., Ding, L., Zhu, W., Zhang, Y., 2022. Synthesis of a novel environmental-friendly biocarbon composite and its highly efficient removal of uranium(VI) and thorium(IV) from aqueous solution. *J. Clean. Prod.* 374, 134059.
39. Lin, C., Wang, H., Wang, Y., Cheng, Z., 2010. Selective solid–phase extraction of trace thorium(IV) using surface-grafted Th(IV)-imprinted polymers with pyrazole derivative. *Talanta* 81, 30–36.
40. Liu, P., Qi, W., Du, Y., Li, Z., Wang, J., Bi, J., Wu, W., 2014. Adsorption of thorium(IV) on magnetic multi-walled carbon nanotubes. *Sci. China Chem.* 57, 1483–1490.
41. Liu, X., Xiao, S., Jin, T., Gao, F., Wang, M., Gao, Y., Zhang, W., Ouyang, Y., Ye, G., 2022. Selective entrapment of thorium using a three-dimensional covalent organic framework and its interaction mechanism study. *Sep. Purif. Technol.* 296, 121413.
42. Liu, X., Zhu, L., Zhao, T., Lan, J., Yan, W., Zhang, H., 2011. Synthesis and characterization of sulfonic acid-functionalized SBA-15 for adsorption of biomolecules. *Microporous Mesoporous Mater.* 142, 614–620.
43. Liu, Z., Ou, T., Su, M., Peng, H., Song, G., Kong, L., Chen, D., 2021. U(VI) sequestration by Al-rich minerals: Mechanism on phase dependence and the influence of natural organic matter. *J. Chem. Eng.* 415, 128858.
44. Luca, V., Hanna, J.V., 2015. A versatile Zr(IV)-organophosphonate coordination polymer platform for the selective adsorption of lanthanides and actinides. *Hydrometallurgy* 154, 118–128.
45. Ma, Y., Xing, L., Zheng, H., Che, S., 2011. Anionic-cationic switchable amphoteric monodisperse mesoporous silica nanoparticles. *Langmuir* 27, 517–520.
46. Marczenko, Z., Balcerzak, M., 2000. Chapter 51-Thorium. In: Marczenko, Z., Balcerzak, M. (Editors), *Analytical Spectroscopy Library*. Elsevier, pp. 424–430.
47. Mastren, T., Radchenko, V., Engle, J.W., Weidner, J.W., Owens, A., Wyant, L.E., Copping, R., Brugh, M., Nortier, F.M., Birnbaum, E.R., John, K.D., Fassbender, M.E., 2018. Chromatographic separation of the theranostic radionuclide <sup>111</sup>Ag from a proton irradiated thorium matrix. *Anal. Chim. Acta* 998, 75–82.
48. Mastren, T., Radchenko, V., Owens, A., Copping, R., Boll, R., Griswold, J.R., Mirzadeh, S., Wyant, L.E., Brugh, M., Engle, J.W., Nortier, F.M., Birnbaum, E.R., John, K.D., Fassbender, M.E., 2017. Simultaneous separation of actinium and radium isotopes from a proton irradiated thorium matrix. *Sci. Rep.* 7, 8216.
49. Mirzabe, G.H., Keshtkar, A.R., 2015. Application of response surface methodology for thorium adsorption on PVA/Fe<sub>3</sub>O<sub>4</sub>/SiO<sub>2</sub>/APTES nanohybrid adsorbent. *J. Ind. Eng. Chem.* 26, 277–285.
50. Moncada, E., Quijada, R., Retuert, J., 2007. Nanoparticles prepared by the sol-gel method and their use in the formation of nanocomposites with polypropylene. *Nanotechnology* 18, 335606.
51. Niculescu, V-C., 2020. Mesoporous silica nanoparticles for bio-applications. *Front. Mater.* 7, 36.
52. Nilchi, A., Dehaghan, T.Sh., Garmarodi, S.R., 2013. Kinetics, isotherm and thermodynamics for uranium and thorium ions adsorption from aqueous solutions by crystalline tin oxide nanoparticles. *Desalination* 321, 67–71.
53. Omar, H.A., Moloukhia, H., 2008. Use of activated carbon in removal of some radioisotopes from their waste solutions. *J. Hazard. Mater.* 157, 242–246.
54. Pal, N., Cho, E-B., Kim, D., 2014. Synthesis of ordered mesoporous silica/ceria–silica composites and their high catalytic performance for solvent-free oxidation of benzyl alcohol at room temperature. *RSC Adv.* 4, 9213–9222.
55. Pool, J.A., Scott, B.L., Kiplinger, J.L., 2005. A new mode of reactivity for pyridine N-oxide: C-H activation with uranium(IV) and thorium(IV) bis(alkyl) complexes. *J. Am. Chem. Soc.* 127, 1338–1339.
56. Proctor, A., Clark, P.K., Parker, C.A., 1995. Rice hull ash adsorbent performance under commercial soy oil bleaching conditions. *J. Am. Oil Chem. Soc.* 72, 459–462.
57. Qasim, M., Singh, B.R., Naqvi, A.H., Paik, P., Das, D., 2015. Silver nanoparticles embedded mesoporous SiO<sub>2</sub> nanosphere: an effective anticandidal agent against *Candida albicans* 077. *Nanotechnology* 26, 285102.
58. Qiu, S., Li, S., Dong, Y., Su, X., Wang, Y., Shen, Y., Sun, X., 2017. A high-performance impregnated resin for recovering thorium from radioactive rare earth waste residue. *J. Mol. Liq.* 237, 380–386.

59. Rahman, N.A., Widhiana, I., Juliastuti, S.R., Setyawan, H., 2015. Synthesis of mesoporous silica with controlled pore structure from bagasse ash as a silica source. *Colloids and Surf., A* 476, 1–7.
60. Rangabhashiyam, S., Anu, N., Nandagopal, M.S.G., Selvaraju, N., 2014. Relevance of isotherm models in biosorption of pollutants by agricultural byproducts. *J. Environ. Chem. Eng.* 2, 398–414.
61. Rellergert, W.G., DeMille, D., Greco, R.R., Hehlen, M.P., Torgerson, J.R., Hudson, E.R., 2010. Constraining the evolution of the fundamental constants with a solid-state optical frequency reference based on the  $^{229}\text{Th}$  nucleus. *Phys. Rev. Lett.* 104, 200802.
62. Rezk, M.M., 2018. A neuro-comparative study between single/successive thorium dose intoxication and alginate treatment. *Biol. Trace Elem. Res.* 185, 414–423.
63. Thambiliyagodage, C.J., Cooray, V.Y., Perera, I.N., Wijesekera, R.D., 2020. Eco-Friendly Porous Carbon Materials for Wastewater Treatment. In: Dissanayake R, Mendis P (Hrsg.), ICSBE 2018. Springer Singapore, Singapore, pp. 252–260.
64. Thirumavalavan, M., Wang, Y-T., Lin, L-C., Lee, J-F., 2011. Monitoring of the structure of mesoporous silica materials tailored using different organic templates and their effect on the adsorption of heavy metal ions. *J. Phys. Chem. C* 115, 8165-8174.
65. Varala S., Ravisankar V., Al-Ali M., Pownceby M.I., Parthasarathy R., Bhargava S.K., 2019, Process optimization using response surface methodology for the removal of thorium from aqueous solutions using rice-husk. *Chemosphere* 237, 124488.
66. Walcarius, A., Mercier, L., 2010. Mesoporous organosilica adsorbents: nanoengineered materials for removal of organic and inorganic pollutants. *J. Mater. Chem.* 20, 4478–4511.
67. Wu, L., Ye, Y., Liu, F., Tan, C., Liu, H., Wang, S., Wang, J., Yi, W., Wu, W., 2013. Organo-bentonite- $\text{Fe}_3\text{O}_4$  poly(sodium acrylate) magnetic superabsorbent nanocomposite: Synthesis, characterization, and thorium(IV) adsorption. *Appl. Clay Sci.* 83–84, 405–414.
68. Xia, T., Yin, L., Xie, Y., Ji, Y., 2020. Efficiently remove of Cs(I) by metals hexacyanoferrate modified magnetic  $\text{Fe}_3\text{O}_4$ -chitosan nanoparticles. *Chem. Phys. Lett.* 746, 137293.
69. Xiong, J., Hu, S., Liu, Y., Yu, J., Yu, H., Xie, L., Wen, J., Wang, X., 2017. Polypropylene modified with amidoxime/carboxyl groups in separating uranium(VI) from thorium(IV) in aqueous solutions. *ACS Sustain. Chem. Eng.* 5, 1924–1930.
70. Xu, J., Zhou, L., Jia, Y., Liu, Z., Adesina, A.A., 2015. Adsorption of thorium (IV) ions from aqueous solution by magnetic chitosan resins modified with triethylene-tetramine. *J. Radioanal. Nucl. Chem.* 303, 347–356.
71. Yang, S., Qian, J., Kuang, L., Hua, D., 2017. Ion-imprinted mesoporous silica for selective removal of uranium from highly acidic and radioactive effluent. *ACS Appl. Mater. Interfaces* 9, 29337–29344.
72. Yang, X-Y., Léonard, A., Lemaire, A., Tian, G., Su, B-L., 2011. Self-formation phenomenon to hierarchically structured porous materials: design, synthesis, formation mechanism and applications. *Chem. Commun.* 47, 2763–2786.
73. Yousefi, S.R., Ahmadi, S.J., Shemirani, F., Jamali, M.R., Salavati-Niasari, M., 2009. Simultaneous extraction and preconcentration of uranium and thorium in aqueous samples by new modified mesoporous silica prior to inductively coupled plasma optical emission spectrometry determination. *Talanta* 80, 212–217.
74. Zhao, M., Cui, Z., Pan, D., Fan, F., Tang, J., Hu, Y., Xu, Y., Zhang, P., Li, P., Kong, X.Y., Wu, W., 2021. An efficient uranium adsorption magnetic platform based on amidoxime-functionalized flower-like  $\text{Fe}_3\text{O}_4@ \text{TiO}_2$  core-shell microspheres. *ACS Appl. Mater. Interfaces*, 13, 17931–17939.
75. Zhu, W., Wang, J., Wu, D., Li, X., Luo, Y., Han, C., Ma, W., He, S., 2017. Investigating the heavy metal adsorption of mesoporous silica materials prepared by microwave synthesis. *Nanoscale Res. Lett.* 12, 323.
76. Zuo, L., Yu, S., Zhou, H., Tian, X., Jiang, J., 2011. Th(IV) adsorption on mesoporous molecular sieves: effects of contact time, solid content, pH, ionic strength, foreign ions and temperature. *J. Radioanal. Nucl. Chem.* 288, 379–387.

## Figures

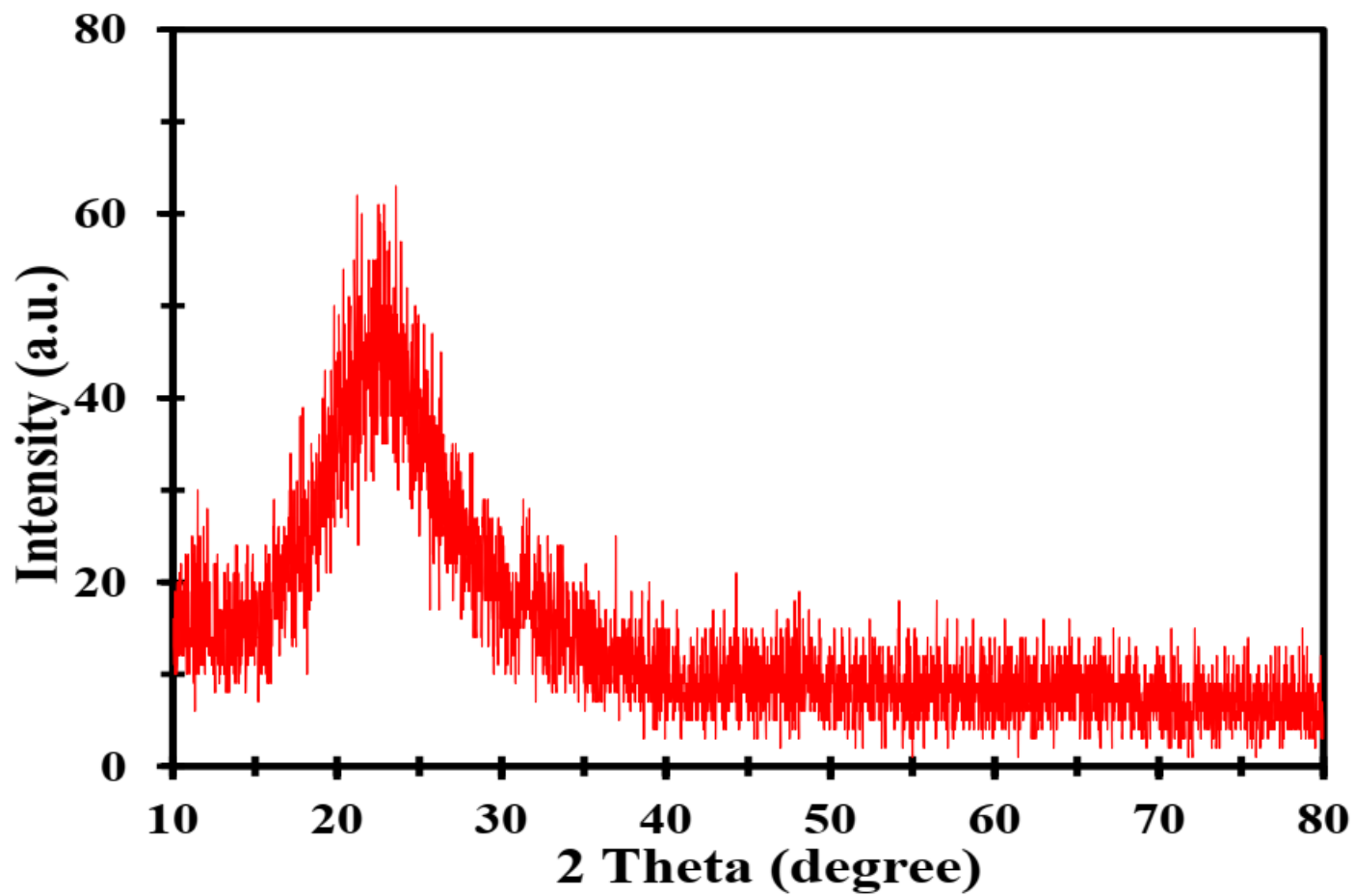


Figure 1

XRD analysis of the mesoporous SBL

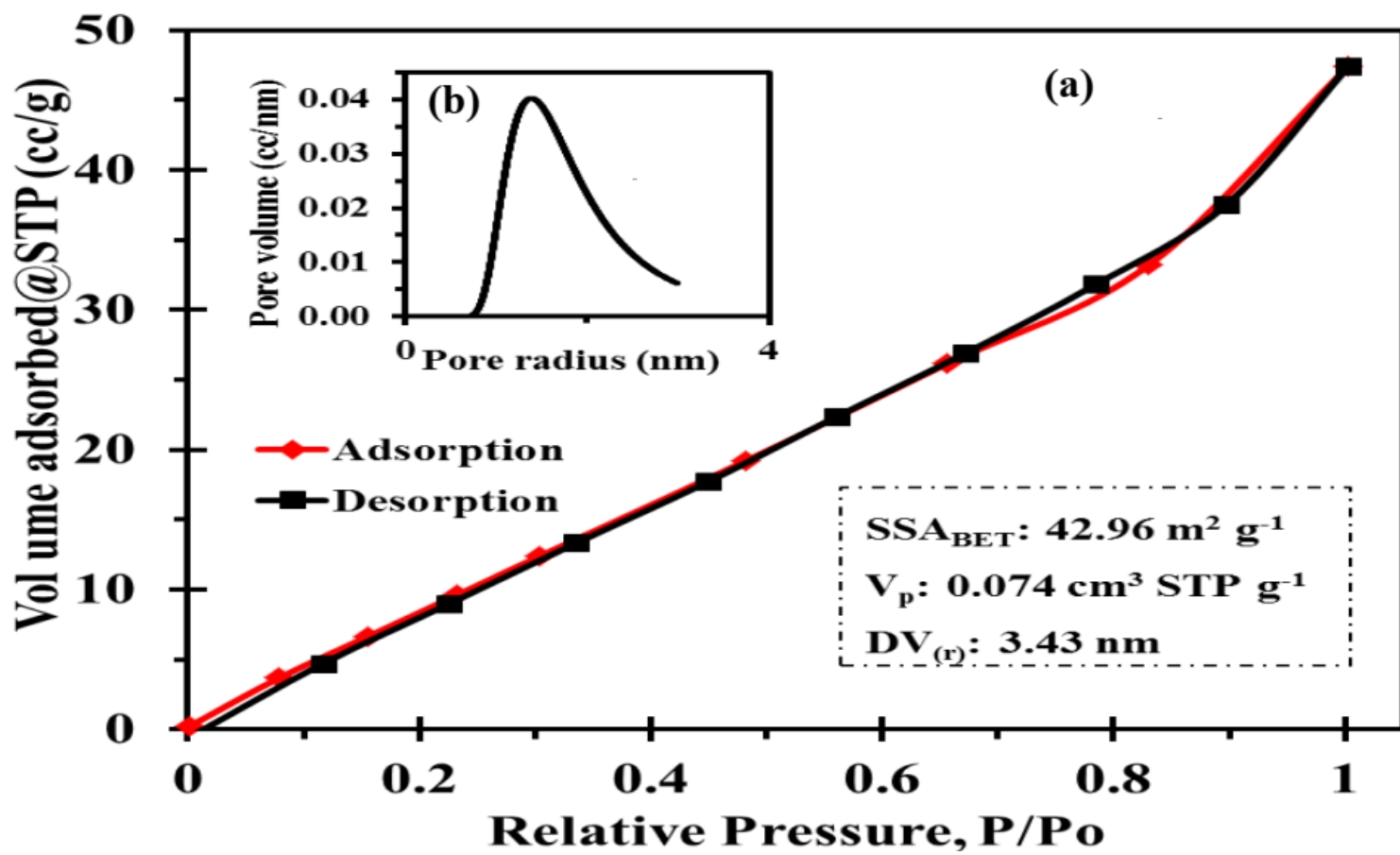
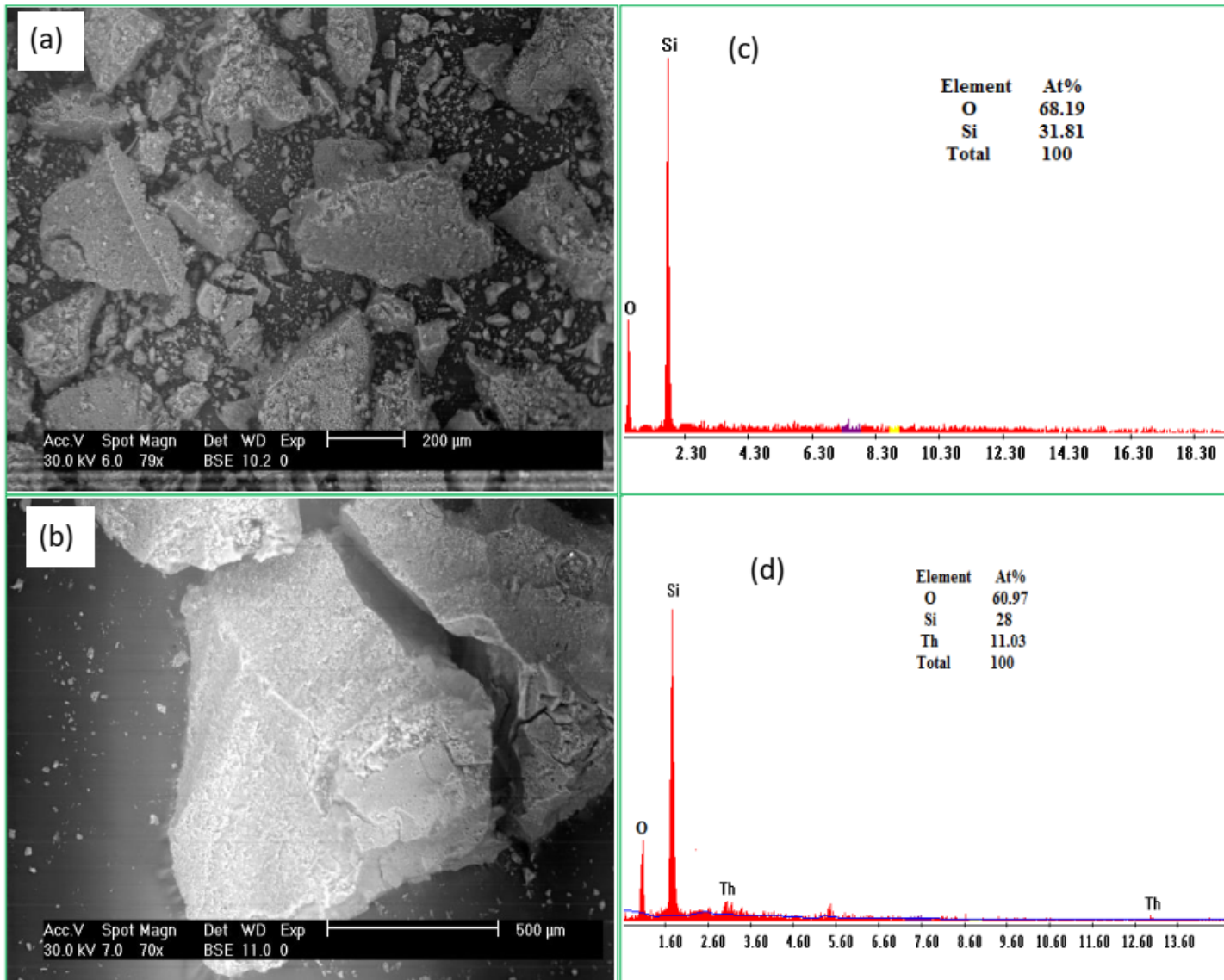


Figure 2

Textural characterization of mesoporous SBL by (a)  $N_2$  adsorption-desorption analysis and (b) pore-size distribution





**Figure 3**

SEM photos of **(a)** SBL, **(b)** Th/SBL, and EDX spectra of **(c)**mesoporous SBL, **(d)** Th/SBL

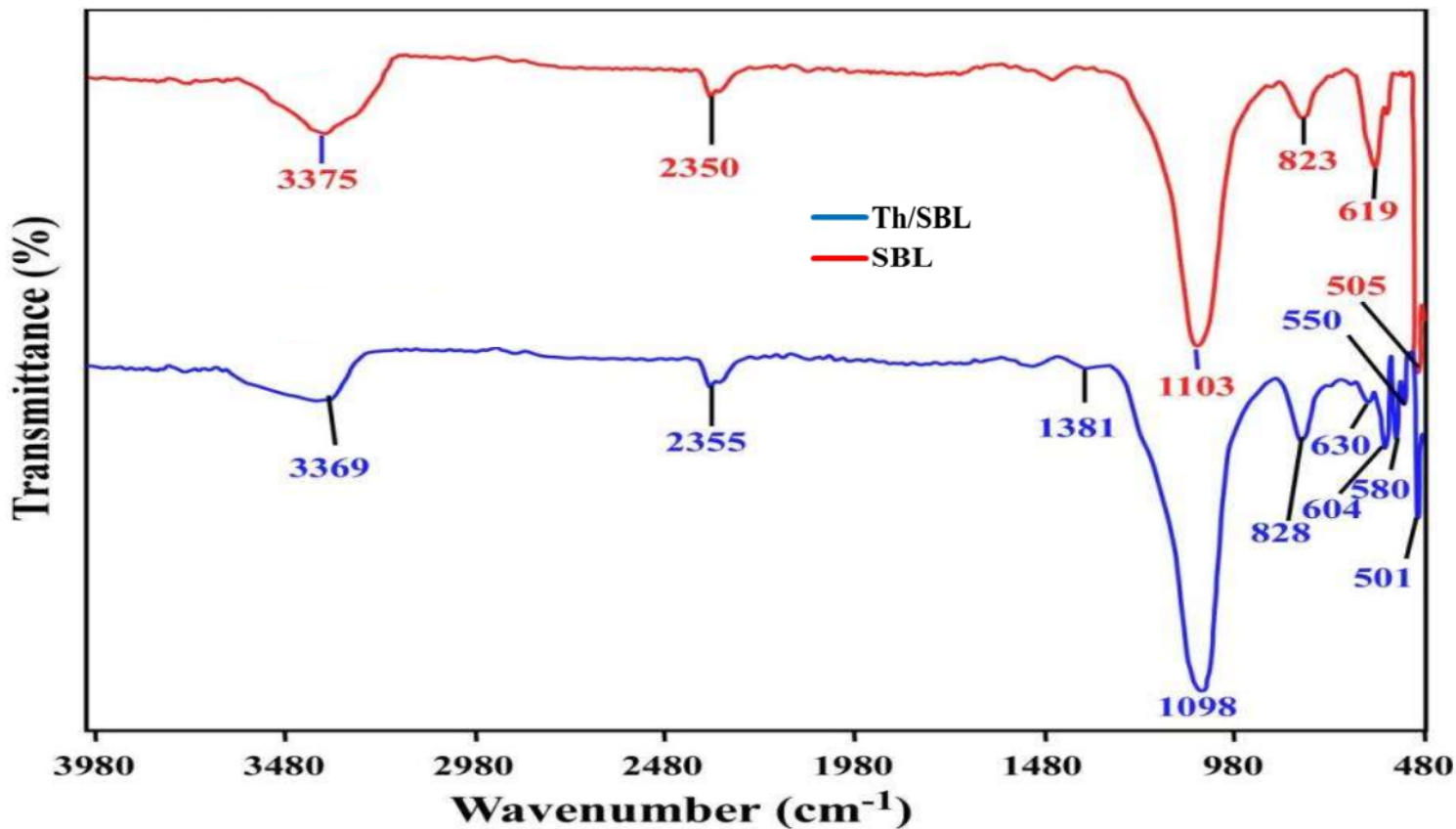


Figure 4

FTIR spectra of mesoporous SBL and Th/SBL

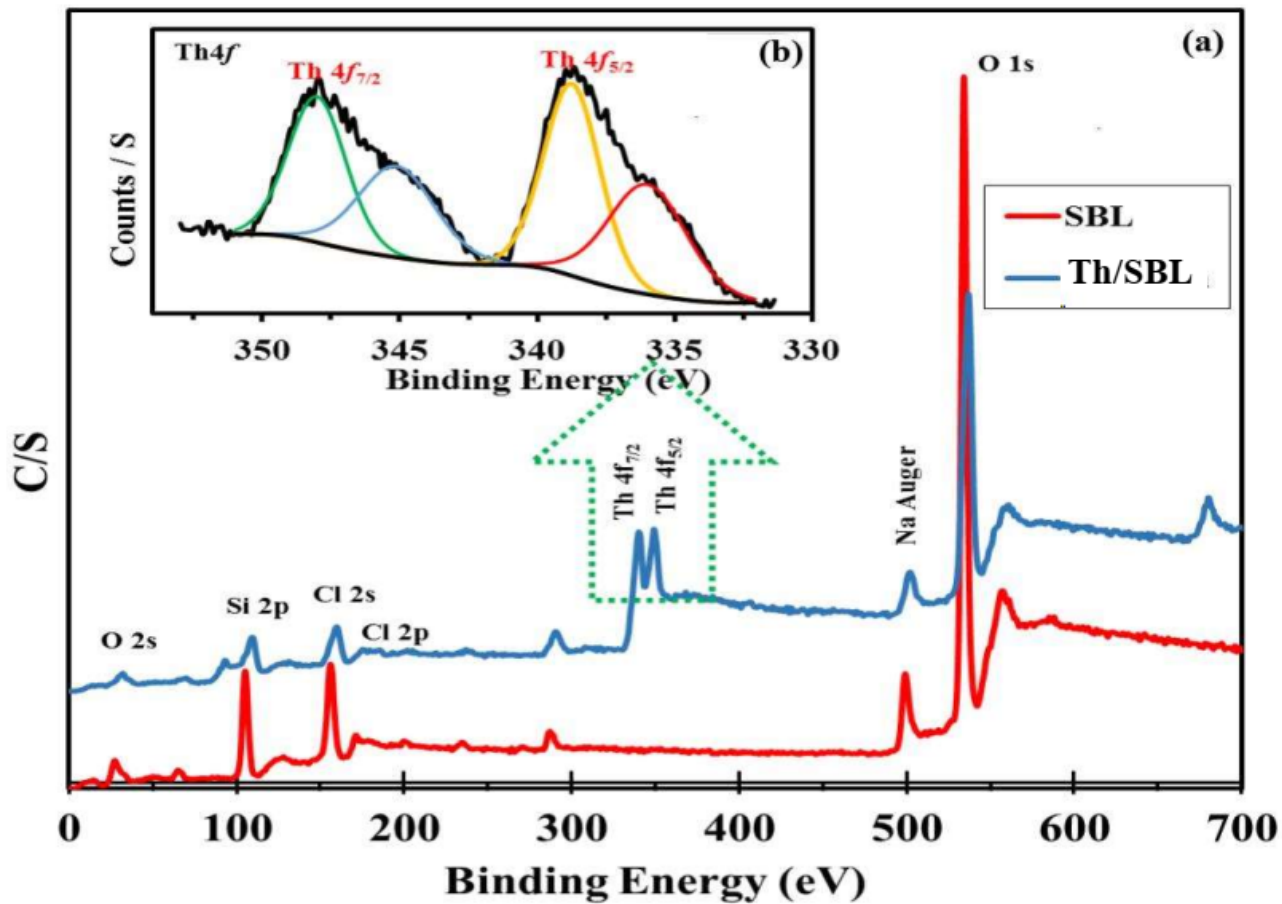


Figure 5

Survey XPS spectra of mesoporous SBL and Th/SBL (a) and XPS spectra of Th 4f for Th/SBL (b)

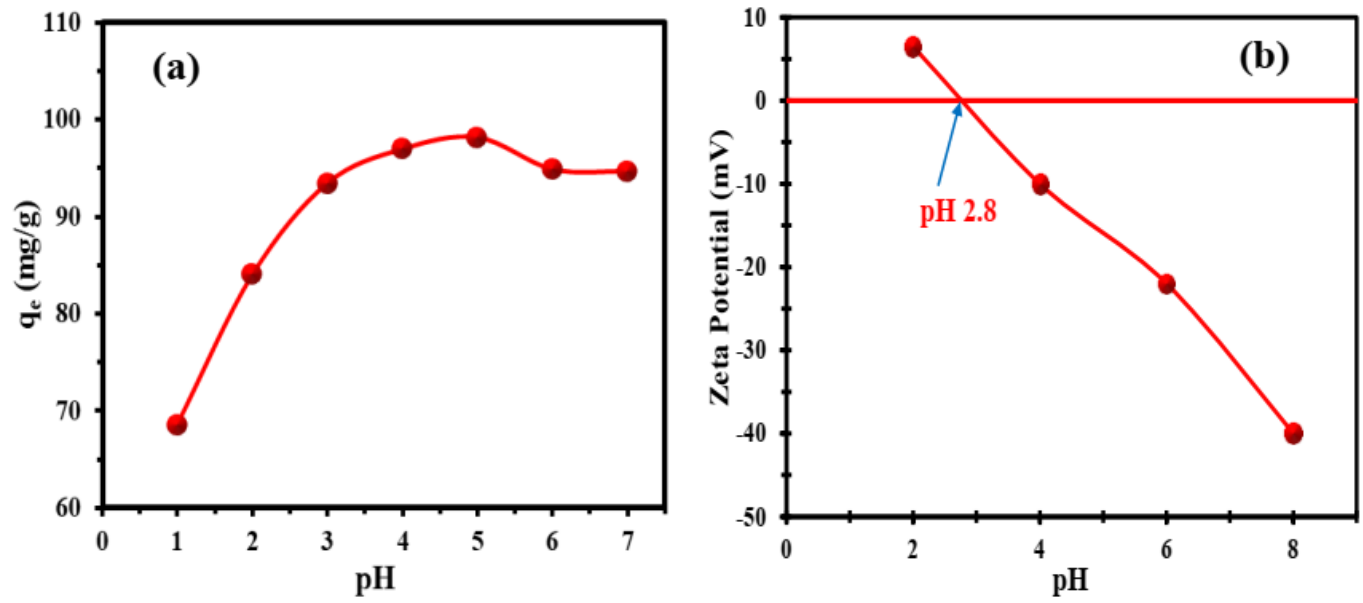


Figure 6

(a) pH impact on the Th(IV) sorption on silica composite, (b) Zeta potential and  $pH_{pzc}$  for SBL sorbent.

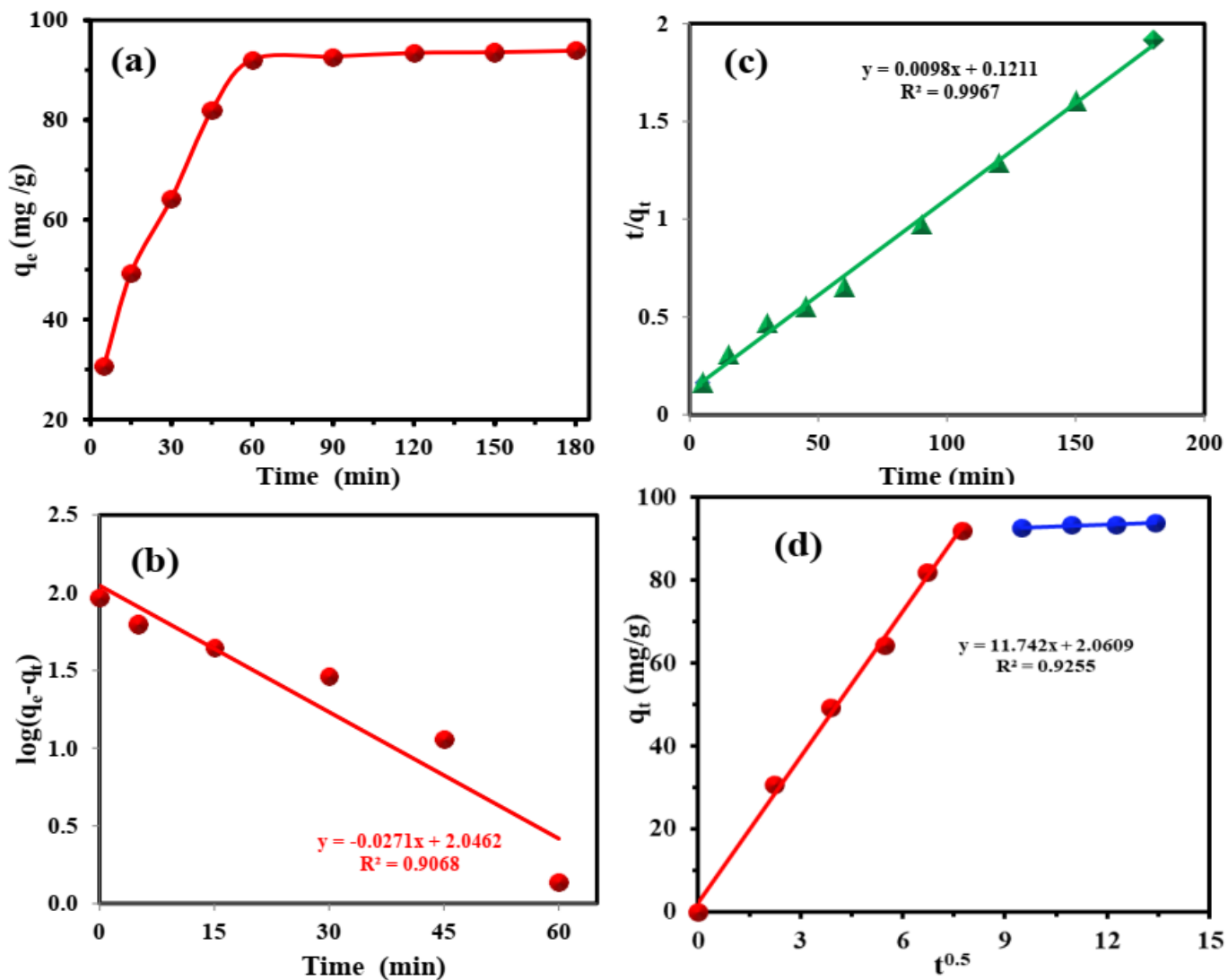


Figure 7

(a) Time effect on Th(IV) sorption on mesoporous SBL, (b) kinetic model of sPFOLE, (c) kinetic model of sPSOLE, (d) kinetic equation of Weber and Morris (sIPDE) for Th(IV) sorption on Mes-Si-NPs

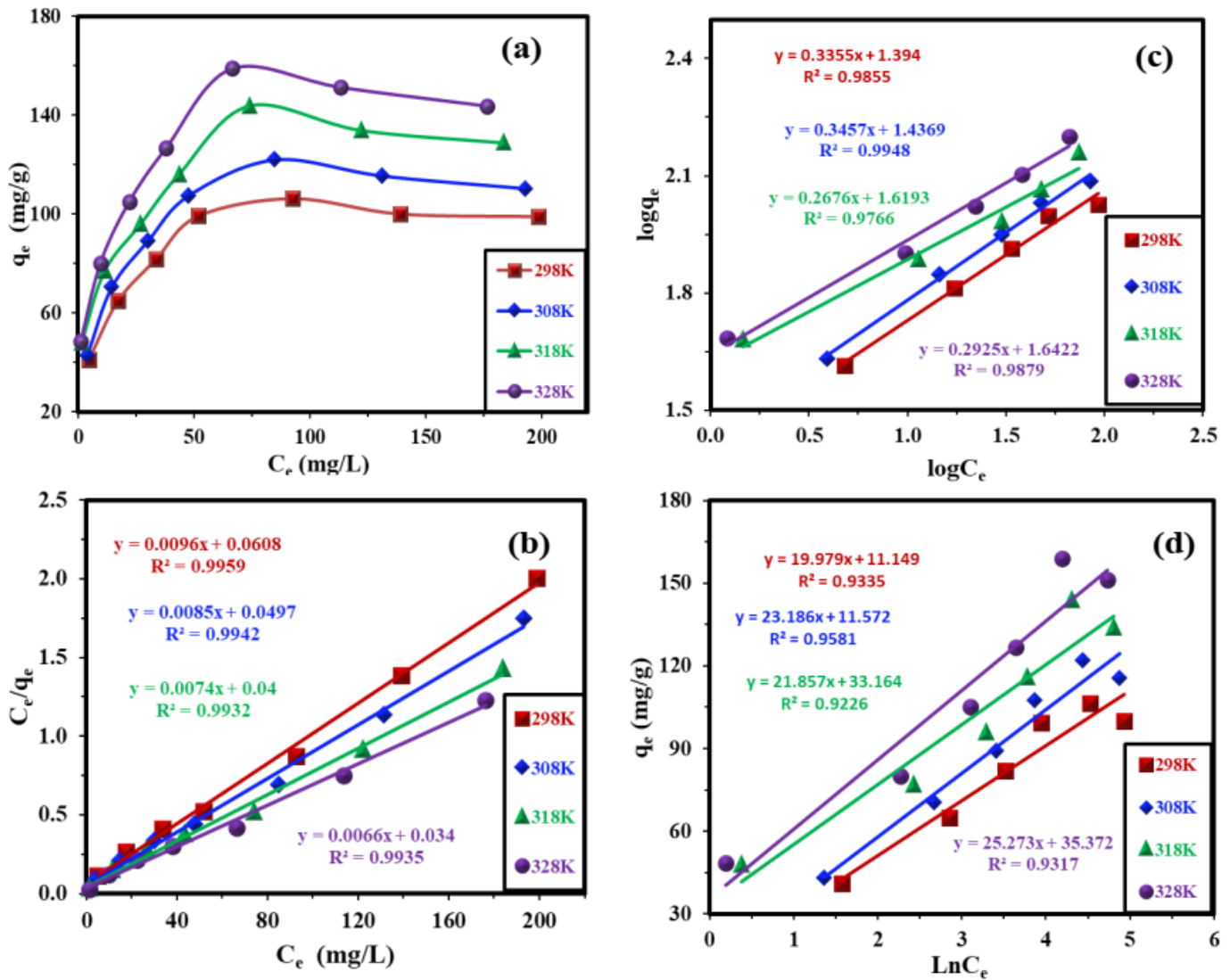


Figure 8

(a) Effect of equilibrium concentration and Th(IV) sorption uptake, (b) Langmuir, (c) Freundlich, (d) Temkin plots for Th(IV) ions sorption

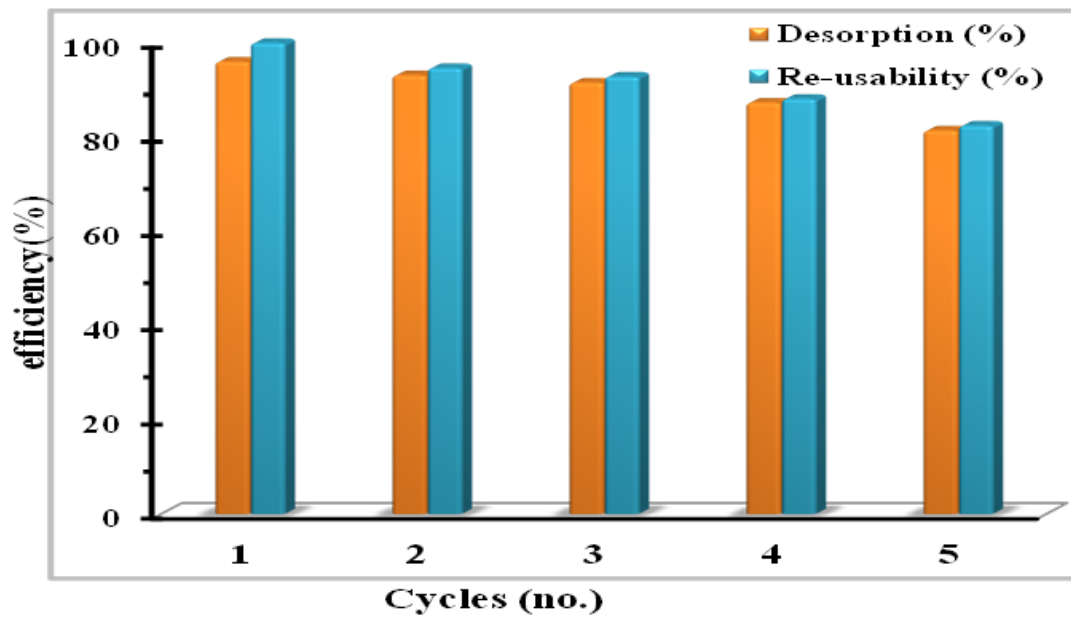


Figure 9

Adsorbent efficiency through desorption and reusability

## Supplementary Files

This is a list of supplementary files associated with this preprint. Click to download.

- [floatimage1.png](#)
- [03ESPRFullArticle.Suppl.docx](#)